
DISTRIBUTION FREE UNCERTAINTY QUANTIFICATION IN NEUROSCIENCE-INSPIRED DEEP OPERATORS

A PREPRINT

Shailesh Garg

Department of Applied Mechanics
Indian Institute of Technology Delhi
Hauz Khas, New Delhi 110016, India.
shailesh.garg@am.iitd.ac.in

Souvik Chakraborty

Department of Applied Mechanics
Yardi School of Artificial Intelligence (YScAI)
Indian Institute of Technology Delhi
Hauz Khas, New Delhi 110016, India.
souvik@am.iitd.ac.in

December 13, 2024

ABSTRACT

Energy-efficient deep learning algorithms are essential for a sustainable future and feasible edge computing setups. Spiking neural networks (SNNs), inspired from neuroscience, are a positive step in the direction of achieving the required energy efficiency. However, in a bid to lower the energy requirements, accuracy is marginally sacrificed. Hence, predictions of such deep learning algorithms require an uncertainty measure that can inform users regarding the bounds of a certain output. In this paper, we introduce the Conformalized Randomized Prior Operator (CRP-O) framework that leverages Randomized Prior (RP) networks and Split Conformal Prediction (SCP) to quantify uncertainty in both conventional and spiking neural operators. To further enable zero-shot super-resolution in UQ, we propose an extension incorporating Gaussian Process Regression. This enhanced super-resolution-enabled CRP-O framework is integrated with the recently developed Variable Spiking Wavelet Neural Operator (VSWNO). To test the performance of the obtained calibrated uncertainty bounds, we discuss four different examples covering both one-dimensional and two-dimensional partial differential equations. Results demonstrate that the uncertainty bounds produced by the conformalized RP-VSWNO significantly enhance UQ estimates compared to vanilla RP-VSWNO, Quantile WNO (Q-WNO), and Conformalized Quantile WNO (CQ-WNO). These findings underscore the potential of the proposed approach for practical applications.

Keywords Variable Spiking Neuron · Operator learning · Wavelet Neural Operator · Spiking Neurons · Uncertainty Quantification

1 Introduction

Machine learning [1–3] in the current day and age has crossed the initiation threshold and has steamrolled its way into various aspects of science and engineering [4–14]. The increasing appearance of the term *scientific machine learning* in literature [15–17] is a testament to the same. A huge chunk of this credit goes to the rapid development of neural network [18–20] algorithms, which have shown tremendous performance across various scientific tasks. Developments like operator learning algorithms [21–24] have made it relatively easier to learn datasets originating from complex partial differential equations, which are often used to model the physical space around us, whether natural or artificial. However, despite the ongoing improvements, their performance is not at par with the gold standard techniques like finite element modeling [25,26]. This is further true for spiking variants of these operator learning algorithms [27,28], a domain that is particularly important from the view of a sustainable future and edge computing. Naturally, a confidence measure that can inform the user as to how reliable a specific output is and what its boundaries/extremes are becomes essential. Such measures can prove instrumental in tasks where some form of decision-making is involved.

Uncertainty associated with the predictions/outputs of an underlying model is usually represented in the form of confidence intervals or uncertainty bounds. These bounds can give Conditional Coverage (CC) or Marginal CC (MCC) [29, 30] depending on the algorithm adopted for Uncertainty Quantification (UQ). To understand this, assume that we have a set of inputs with n_s samples, and we have uncertainty bounds corresponding to each sample. Then CC implies that for all samples individually, the probability that the corresponding true value will lie within their stipulated bounds is $\geq 1 - \alpha$, $\alpha \in (0, 1)$ being the miscoverage level or error rate. MCC, on the other hand, is applicable to the whole population and states that among all n_s samples's true values, $\geq n_s(1 - \alpha)$ true values should lie between their uncertainty bounds. Although CC is more powerful than MCC, getting bounds that satisfy CC within neural network algorithms is non-trivial [31, 32]. Therefore, the focus is often on developing algorithms that yield MCC. Unfortunately, this is often rendered ineffective because of the inherent assumptions associated with the algorithms. For example, in Bayesian approaches for UQ [33–35], we often assume some prior distribution and make assumptions about the noise present in the system. In frequentist ensemble approaches as well, in order to report bounds that give coverage with probability $\geq 1 - \alpha$, we have to take the Gaussian assumption. Such assumptions, coupled with imperfect optimization of the underlying model, lead to imperfect uncertainty bounds.

To tackle this challenge, researchers use UQ techniques like Conformal Prediction [29, 30, 36] (CP). CP is a distribution-free UQ technique that provides bounds that satisfy MCC conditions without the underlying strong assumptions, as in the case of Bayesian approaches. In this paper, we propose a Conformalized Randomized Prior Operator (CRP-O) framework for UQ. The proposed framework utilizes the concept of Randomized Prior (RP) networks [37] and extends it to a base neural operator in order to arrive at a heuristic measure of uncertainty. This initial estimate is then calibrated using Split CP [29, 30, 36] to get the desired coverage using the estimated uncertainty and, hence, to satisfy the MCC condition. The motivation for adopting the RP networks to arrive at an initial heuristic estimate of uncertainty is that while being set in a deterministic framework, it also allows users to incorporate any prior information regarding the dataset, and it is trivial to implement even for complex architectures. We have further enhanced the CRP-O framework by exploiting a Gaussian Process to enable zero-shot super-resolution in UQ. The proposed enhanced CRP-O framework is used in conjunction with the Variable Spiking Wavelet Neural Operator [27] (VSWNO), which is a spiking variant of vanilla Wavelet Neural Operator [23] (WNO) architecture. The applicability of the CRP-O framework is also shown when vanilla WNO is used as the base operator.

We note that there are two prior work that have proposed conformal prediction in neural operator. Moya *et al.* [31] proposed a UQ technique for Deep Operator Network [21] (DeepONet) architecture using SCP, and it proposes the use of quantile regression for training the base operator. Ma *et al.* [32] proposed Risk-Controlling Quantile Neural Operator (RCQNO) that relies on quantile regression for obtaining the initial uncertainty estimates and couples it with SCP. However, quantile regression often suffer from crossing quantiles, that can reduce the effectiveness of SCP. Furthermore, (RCQNO) [32] requires splitting the available datasets into three different parts, which can be problematic for applications with limited data.

Four examples are discussed to test the efficacy of the proposed approach, and we compare the coverage of uncertainty bounds obtained using the CRP-VSWNO/ CRP-WNO with those obtained using vanilla RP-VSWNO/ RP-WNO [38], Q-WNO, and conformalized Q-WNO (CQ-WNO). The results produced show that while the latter fails to satisfy the MCC condition, the former gives the required coverage for the test dataset when analyzed as a whole. A comparison of the performance of conformalized RP-WNO is also drawn against the performance of RCQNO. The highlights of the proposed framework include,

- **Application to VSWNO:** In this paper, we show the applicability of the proposed framework to VSWNO. Spiking neural networks promise a more energy-efficient approach to deep learning, but because of their inherent sparse communication, the accuracy achieved is slightly affected. Thus, it becomes important to quantify the uncertainty associated with their predictions, and the proposed framework is able to capture the same effectively.
- **RP-Operator as the heuristic measure of uncertainty:** RP-Operator as an initial uncertainty estimator has the advantage of being set in a deterministic framework, which allows users to implement it for complex datasets easily. It can also incorporate prior information regarding the dataset, which is often omitted in a deterministic framework. It should be noted that despite its trivial nature, the underlying uncertainty estimates are robust enough that with the help of a meager calibration dataset, they can be improved to provide better coverage, and its mean predictions give a good approximation of the ground truth.
- **Limited data split:** The proposed framework requires the original dataset to be split into only two parts, (i) the training dataset and (ii) the calibration dataset. This is helpful in cases where the dataset available is sparse and limited.

- **Super-resolution predictions:** In this paper, using the Gaussian process [39, 40], we show how the proposed framework can be extended for uncertainty quantification in super-resolution predictions of RP operator networks.

The rest of the paper is arranged as follows. Section 2 discusses the instances from literature where SCP is used for UQ in operator learning. Section 3 details the proposed framework, and section 4 shows the numerical illustrations. Section 5 concludes the findings of the paper.

2 Related Works

In this section, we discuss the available literature on how the SCP algorithm is used for UQ in operator learning algorithms. The goal of the SCP algorithm is to provide uncertainty bounds that satisfy the MCC condition for a given trained network’s output. Formally, given a calibration dataset having n i.i.d. input-output pairs (\mathbf{u}_i, y_i) , $\mathbf{u}_i \in \mathbb{R}^d$, $y_i \in \mathbb{R}$ and a test sample pair (\mathbf{u}_t, y_t) , we want a prediction band $\mathcal{C}_p(\mathbf{u}_t)$ that satisfies,

$$\mathbb{P}(y_t \in \mathcal{C}_p(\mathbf{u}_t)) \geq 1 - \alpha, \quad (1)$$

where the probability $\mathbb{P}(\cdot)$ is computed over the $n + 1$ i.i.d pair of samples. To achieve this, we require a heuristic measure of uncertainty, which is then modified to obtain the required bands.

2.1 Conformal Quantile DeepONet Regression

Proposed in [31], the conformal quantile DeepONet regression framework utilizes DeepONet [21] architecture to arrive at the base heuristic estimate of uncertainty and then utilizes SCP to calibrate the same and to provide the desired coverage. Two copies of the DeepONet model are trained on the same dataset using quantile regression [41, 42], one for $\alpha/2$ quantile and the other for $1 - \alpha/2$ quantile. To train the network for λ quantile, a pinball loss $L_p(y, y_{p_\lambda})$ function is used, and the same is defined as,

$$L_p(y, y_{p_\lambda}) = \begin{cases} \lambda(y - y_{p_\lambda}), & y - y_{p_\lambda} > 0 \\ (1 - \lambda)(y_{p_\lambda} - y), & y - y_{p_\lambda} \leq 0 \end{cases}, \quad (2)$$

where y is the true value and y_{p_λ} is the model prediction when training for λ quantile. Upon training the two base models, an initial confidence interval set is formed. The same is then calibrated using the SCP algorithm and a calibration dataset. The results shown in [31] illustrate that, on an average, the framework yields the desired coverage; however, the coverage obtained falls short at a few locations in the solution’s domain. Furthermore, quantile regression suffers from crossing quantiles, which is not addressed in [31]. As shown in the current paper, the quantile training for WNO architecture produces sub-par results that, while improved upon calibration, still fall short of providing desired coverage at all locations of the solution domain.

2.2 Risk-Controlling Quantile Neural Operator

The paper [32] proposes RCQNO to obtain (α, δ) risk-controlling prediction set that has two main components: (i) base operator and (ii) pre-calibration quantile neural operator. Fourier neural operator [22] is used as the background operator algorithm in this paper. The idea here is to first train the base operator using a training dataset D_{tr_I} . Afterward, using the trained base operator, residuals $|y - y_p|$ are computed corresponding to a different training dataset $D_{tr_{II}}$. The residuals and their corresponding inputs are used to train a new pre-calibration neural operator model with the goal of learning the point-wise radius of an assumed uncertainty ball corresponding to a given input function. Quantile regression is used to train this pre-calibration neural operator model. This point-wise radius forms the initial heuristic measure of uncertainty, which is then calibrated using a variant of SCP algorithm and a calibration dataset. This approach requires the dataset to be split into three portions, which is problematic for scenarios where the dataset is limited. Furthermore, the hyper-parameters used while calibrating the point-wise radius in the proposed algorithm of the paper greatly affect the amount of calibration dataset required, putting further strain on the already stretched dataset.

3 Proposed approach

In this section, we provide details of the proposed Conformalized RP Operator (CRP-O) for enabling uncertainty quantification with guaranteed MCC. In particular, we have two technical contributions. First, we hypothesize that the initial uncertainty estimates have a significant effect on the performance of the SCP algorithm. To that end, we propose

to use RP networks to estimate the base uncertainty. The advantages of RP networks over other alternatives such as Bayesian, quantile, and ensemble include their computational efficiency when parallelized, their scalability to complex neural network architectures, and their ability to account for prior information while being set in a deterministic framework. Second, one of the key features of neural operators is super-resolution. Here, we propose a GP based UQ framework that extends the CRP-O framework to enable UQ when predicting outputs at a resolution different from the one used during training. a UQ framework for spiking neural operators does not exist in the available literature. We integrate the proposed framework with recent proposed VSWNO [27] to illustrate how the proposed approach can enable UQ in neuroscience inspired operators. To our knowledge, this is the first attempt towards developing an UQ enabled neuroscience inspired neural operator. We first briefly review VSWNO, a spiking variant of the vanilla WNO, and then proceed to introduce the CRP-O framework and, subsequently, the GP-based approach for enabling UQ in super-resolution.

3.1 Variable spiking WNO (VSWNO)

VSWNO [27] is an energy-efficient variant of vanilla WNO (refer A for details on WNO) that exhibits event-driven computation behavior and sparse communication. To achieve this, it utilizes neuroscience-inspired Variable Spiking Neurons [43] (VSNs) within its architecture. Specifically, the continuous activations $\sigma(\cdot)$ of artificial neurons used in vanilla WNO architecture are replaced by Variable Spiking Neurons [43] (VSNs), giving rise to sparse communication and hence energy efficiency. The dynamics of a VSN is defined as follows,

$$\begin{aligned} \mathcal{M}_t &= \beta_l \mathcal{M}_{t-1} + z_t, \\ \tilde{y} &= \begin{cases} 1, & \mathcal{M}_t \geq T_h \\ 0, & \mathcal{M}_t < T_h \end{cases}, \\ &\text{if } \tilde{y} = 1, \mathcal{M}_t \leftarrow 0, \\ y_t &= \sigma(\tilde{y} z_t), \text{ given } \sigma(0) = 0, \end{aligned} \quad (3)$$

where y_t is the output of VSN corresponding to the input z_t at the t^{th} time step of the input spike train. \mathcal{M}_t represents the memory of the VSN at the t^{th} time step of the spike train. β_l and T_h are the leakage and threshold parameters of the VSN, which can be treated as trainable parameters during network training. [27] shows that VSWNO is able to produce results comparable to vanilla WNO with only a single time step in the spike train. Because the dynamics of VSN involve discontinuity in the form of hard threshold function, while training VSWNO, surrogate backpropagation [43, 44] is used. In surrogate backpropagation, during the backward pass of network training, the hard threshold function is idealized using an approximate smooth function, thus enabling gradient calculation. As discussed previously, we use the VSWNO in conjunction with RP networks to obtain our base estimate of the uncertainty in the proposed CRP-O framework.

3.2 Conformalized RP operator (CRP-O)

The CRP-O framework comprises two key components: Randomized Prior (RP) networks and the Stochastic Cross-Validation Procedure (SCP) algorithm. The RP networks employ an ensemble-based training approach, enabling uncertainty quantification within a deterministic framework. This setup ensures straightforward implementation, even for complex deep learning architectures. Notably, RP networks extend beyond vanilla ensemble methods by incorporating prior information about the dataset under consideration.

The training process for RP networks involves optimizing n_c copies of the base network, each augmented with a prior network. Mathematically, let $\mathcal{L}(\theta; \mathcal{D})$ represent the loss function for the dataset \mathcal{D} , where θ denotes the network parameters. For each copy $k \in \{1, 2, \dots, n_c\}$, the augmented loss is defined as:

$$\mathcal{L}_{\text{aug}}^{(k)}(\theta^{(k)}; \mathcal{D}) = \mathcal{L}(\theta^{(k)}; \mathcal{D}) + \lambda \mathcal{L}_{\text{prior}}(\phi), \quad (4)$$

where $\mathcal{L}_{\text{prior}}(\phi)$ encodes prior knowledge through a non-trainable prior network with parameters ϕ , and λ is a weighting factor controlling the influence of the prior. Each of the n_c augmented networks is initialized with different random seeds but trained on the same dataset \mathcal{D} . The prior network, typically a neural network with an architecture similar to the base network, has fixed, non-trainable parameters. The incorporation of prior information can also take the form of known physics or domain-specific constraints. This ensemble-based approach not only enhances robustness but also facilitates seamless integration of domain knowledge into the learning process, making RP networks a powerful tool for uncertainty-aware predictions.

In this paper, we use the term **RP operator** to signify the application of the RP network framework to neural operator algorithms. When the base operator network within the RP operator is chosen as the Variable-Width Spectral Neural

Operator (VSWNO), the resulting model is denoted as **RP-VSWNO**. Similarly, if the base operator network is the standard Wavelet Neural Operator (WNO), the resulting model is referred to as **RP-WNO**. For RP-VSWNO, the prior network can either be an instance of VSWNO or a simpler WNO model. In this work, we use a smaller WNO model as the prior network for RP-VSWNO. Once the RP operator is trained, given an input \mathbf{u}_t , the outputs $y_{p(i)}(\mathbf{u}_t)$, $i = 1, \dots, n_c$ are collected from all n_c copies of the operator network. The final mean $\mu(\mathbf{u}_t)$ and standard deviation $s(\mathbf{u}_t)$ are computed as:

$$\mu(\mathbf{u}_t) = \frac{1}{n_c} \sum_{i=1}^{n_c} y_{p(i)}(\mathbf{u}_t), \quad (5a)$$

$$s(\mathbf{u}_t) = \sqrt{\frac{1}{n_c} \sum_{i=1}^{n_c} (\mu(\mathbf{u}_t) - y_{p(i)}(\mathbf{u}_t))^2}. \quad (5b)$$

For non-scalar outputs, the above computations are performed element-wise for each dimension of the multi-dimensional output. Using the computed mean and standard deviation, the RP operator provides an initial confidence interval for a given input \mathbf{u}_t as:

$$\mathcal{C}_{\text{ini}}(\mathbf{u}_t) = [\mu(\mathbf{u}_t) - zs(\mathbf{u}_t), \mu(\mathbf{u}_t) + zs(\mathbf{u}_t)], \quad (6)$$

where z is a parameter determined by the desired confidence level. The initial uncertainty estimate \mathcal{C}_{ini} from the RP operator is further calibrated using the SCP algorithm. The final calibrated prediction band \mathcal{C}_p is defined as:

$$\mathcal{C}_p(\mathbf{u}_t) = [\mu(\mathbf{u}_t) - zqs(\mathbf{u}_t), \mu(\mathbf{u}_t) + zqs(\mathbf{u}_t)], \quad (7)$$

where the parameter q is computed using the SCP algorithm. To determine q , the trained RP operator is applied to a calibration dataset $\{\mathbf{u}_i, y_i\}_{i=1}^n$ (distinct from the training dataset). For each calibration sample, the mean and standard deviation are obtained using Eq. (5), and a score function e is computed as:

$$e_i(\mathbf{u}_i, y_i) = \frac{|y_i - \mu(\mathbf{u}_i)|}{s(\mathbf{u}_i)}. \quad (8)$$

For non-scalar outputs, the score function is calculated separately for each point in the output domain. The parameter q is then defined as the quantile of the score values over the calibration dataset:

$$q = \text{Quantile} \left(\{e_1, e_2, \dots, e_n\}, \frac{\lceil (1 - \alpha)(n + 1) \rceil}{n} \right), \quad (9)$$

where $\text{Quantile}(\mathcal{A}, a)$ represents the a -quantile of the set \mathcal{A} , and α corresponds to the desired confidence level. To ensure distinct score function values for the calibration dataset with high probability, jitter values can be added as necessary.

Lemma 1 *The SCP algorithm provides calibrated prediction intervals such that for any arbitrary score function $e(\mathbf{u}, y)$ that correctly estimates the discrepancy between predictions and true values, the probability of the true output y_t lying within the calibrated interval $\mathcal{C}_p(\mathbf{u}_t)$ satisfies the guarantee:*

$$\mathbb{P}(y_t \in \mathcal{C}_p(\mathbf{u}_t)) \geq 1 - \alpha,$$

for $\alpha \geq \frac{1}{n+1}$, where n is the size of the calibration dataset.

Proof: Let the score function values $\{e_i\}_{i=1}^n$ computed for the calibration dataset $\{\mathbf{u}_i, y_i\}_{i=1}^n$ be sorted in increasing order as:

$$e_1 \leq e_2 \leq \dots \leq e_n. \quad (10)$$

For a desired confidence level $1 - \alpha$, the parameter q is chosen as:

$$q = e_{\lceil (1 - \alpha)(n + 1) \rceil}. \quad (11)$$

Given this choice of q , the event $y_t \in \mathcal{C}_p(\mathbf{u}_t)$ is equivalent to $e_t \leq q$, i.e.,

$$\{y_t \in \mathcal{C}_p(\mathbf{u}_t)\} = \{e_t \leq e_{\lceil (1 - \alpha)(n + 1) \rceil}\}. \quad (12)$$

Under the assumption that the calibration samples $\{(\mathbf{u}_i, y_i)\}$ are independent and identically distributed (i.i.d.), the distribution of e_t for a test sample (\mathbf{u}_t, y_t) matches that of the calibration scores $\{e_i\}_{i=1}^n$. Thus, the probability of $e_t \leq e_i$ is given by:

$$\mathbb{P}(e_t \leq e_i) = \frac{i}{n + 1}, \quad i \in \{1, 2, \dots, n\}. \quad (13)$$

From this, the probability of $e_t \leq e_{\lceil(1-\alpha)(n+1)\rceil}$ is:

$$\mathbb{P}(e_t \leq e_{\lceil(1-\alpha)(n+1)\rceil}) = \frac{\lceil(1-\alpha)(n+1)\rceil}{n+1}. \quad (14)$$

By construction of $\lceil \cdot \rceil$, it follows that:

$$\frac{\lceil(1-\alpha)(n+1)\rceil}{n+1} \geq 1-\alpha. \quad (15)$$

Therefore, the probability of y_t lying within the calibrated prediction interval is:

$$\mathbb{P}(y_t \in \mathcal{C}_p(\mathbf{u}_t)) = \mathbb{P}(e_t \leq e_{\lceil(1-\alpha)(n+1)\rceil}) \geq 1-\alpha. \quad (16)$$

For the special case where $\alpha < \frac{1}{n+1}$, the choice $q = \infty$ ensures that all $e_t \leq q$, leading to $\mathbb{P}(y_t \in \mathcal{C}_p(\mathbf{u}_t)) = 1$. Hence, the guarantee is trivially satisfied. For more details on SCP and its proof, readers may follow [29]. \square

We note that VSWNO (or vanilla WNO), being an operator, processes multidimensional outputs obtained by discretizing the output function across spatial and temporal domains. Consequently, the SCP algorithm discussed earlier is applied element-wise to each element of the operator network's output. For instance, consider a two-dimensional output where $\mathbf{y} \in \mathbb{R}^{d_x \times d_y}$. In this case, the algorithm computes $d_x \times d_y$ distinct values of the parameter q , one for each element of the output matrix. The detailed steps for computing the uncertainty bounds for multidimensional outputs are provided in Algorithm 1. Additionally, a schematic representation of the proposed framework is illustrated in Fig. 1.

Algorithm 1 Algorithm for computing uncertainty set \mathcal{C}_p .

Require: Calibration dataset $D_C = \{\mathbf{u}_i, \mathbf{y}_i\}_{i=1}^n$, trained RP-WNO/ RP-VSWNO model, test input \mathbf{u}_t .

- 1: Obtain $\boldsymbol{\mu}(\mathbf{u}_i)$ and $\mathbf{s}(\mathbf{u}_i)$ using trained RP-WNO/ RP-VSWNO for each sample in the calibration dataset.
- 2: Compute score function e_i for each sample of calibration dataset, using $e_i = |\mathbf{y}_i - \boldsymbol{\mu}(\mathbf{u}_i)| \oslash \mathbf{s}_i$, where \oslash represents element-wise division.
- 3: **for** $j = 1$: no. of discretizations of solution grid **do**
- 4: Prepare a vector \mathbf{v} containing magnitudes of j^{th} element of score functions $e_i, i = 1, \dots, n$.
- 5: Conformal parameter q_j corresponding to j^{th} element of output is equal to $\lceil(1-\alpha)(n+1)\rceil/n^{\text{th}}$ quantile of vector \mathbf{v} .
- 6: **end for**
- 7: $\mathbf{q} = \{q_1, q_2, \dots, q_{n_e}\}$, where $n_e = \text{numbers of elements in the solution grid}$.
- 8: Reshape \mathbf{q} to have the same shape as outputs $\boldsymbol{\mu}(\mathbf{u}_t)$ (or $\mathbf{s}(\mathbf{u}_t)$).
- 9: $\mathcal{C}_p = [\boldsymbol{\mu}(\mathbf{u}_t) - \mathbf{s}(\mathbf{u}_t) \circ \mathbf{q}, \boldsymbol{\mu}(\mathbf{u}_t) + \mathbf{s}(\mathbf{u}_t) \circ \mathbf{q}]$, where \circ represents elementwise multiplication.

Output: Calibrated uncertainty set $\mathcal{C}_p(\mathbf{u}_t)$.

3.3 Super-resolution predictions

A key feature of operator learning algorithms is their ability to predict outputs at resolutions different from the training resolution. However, such super-resolution predictions are inherently more error-prone, making it essential to quantify the associated uncertainty. To extend the proposed UQ framework in super-resolution setup, we leverage a Gaussian Process (GP) model [40,45]. First, the parameter q_i is computed for each location $\mathbf{x}_{\text{tr}_i} \in \mathbb{R}^d$ on the initial solution grid \mathcal{G}_{tr} (refer to Algorithm 1). These computed values are then mapped to the corresponding locations $\mathbf{x}_{\text{sr}_i} \in \mathbb{R}^r, r > d$ on the super-resolution solution grid \mathcal{G}_{sr} using the Gaussian Process.

Given a function $q = f(\mathbf{x})$ with q being the conformal parameter, a Gaussian Process (GP) defines a distribution over this function as:

$$f(\mathbf{x}) \sim GP(M(\mathbf{x}; \boldsymbol{\theta}_M), K(\mathbf{x}, \mathbf{x}'; \boldsymbol{\theta}_K)), \quad (17)$$

where $M(\mathbf{x}; \boldsymbol{\theta}_M)$ and $K(\mathbf{x}, \mathbf{x}'; \boldsymbol{\theta}_K)$ denote the mean function and covariance function, respectively. The parameters of these functions are represented by $\boldsymbol{\theta}_M$ and $\boldsymbol{\theta}_K$. Considering zero-mean Gaussian Process, we have:

$$f(\mathbf{x}) \sim GP(0, K(\mathbf{x}, \mathbf{x}'; \boldsymbol{\theta}_K)). \quad (18)$$

Given a set of input locations $\hat{\mathbf{x}} = \{\mathbf{x}_1, \dots, \mathbf{x}_d\}$ and corresponding outputs $\mathbf{q} = \{q_1, \dots, q_d\}$, the GP defined in Eq. (18) reduces to

$$p(f|\hat{\mathbf{x}}) \sim \mathcal{N}(f|\mathbf{0}, \mathbf{K}), \quad (19)$$

where \mathbf{K} represents the covariance matrix. Note that the hyperparameters, $\boldsymbol{\theta}_K$ of \mathbf{K} includes the length-scale parameter and the process variance, which are obtained by maximizing the marginal likelihood (or minimizing the negative log

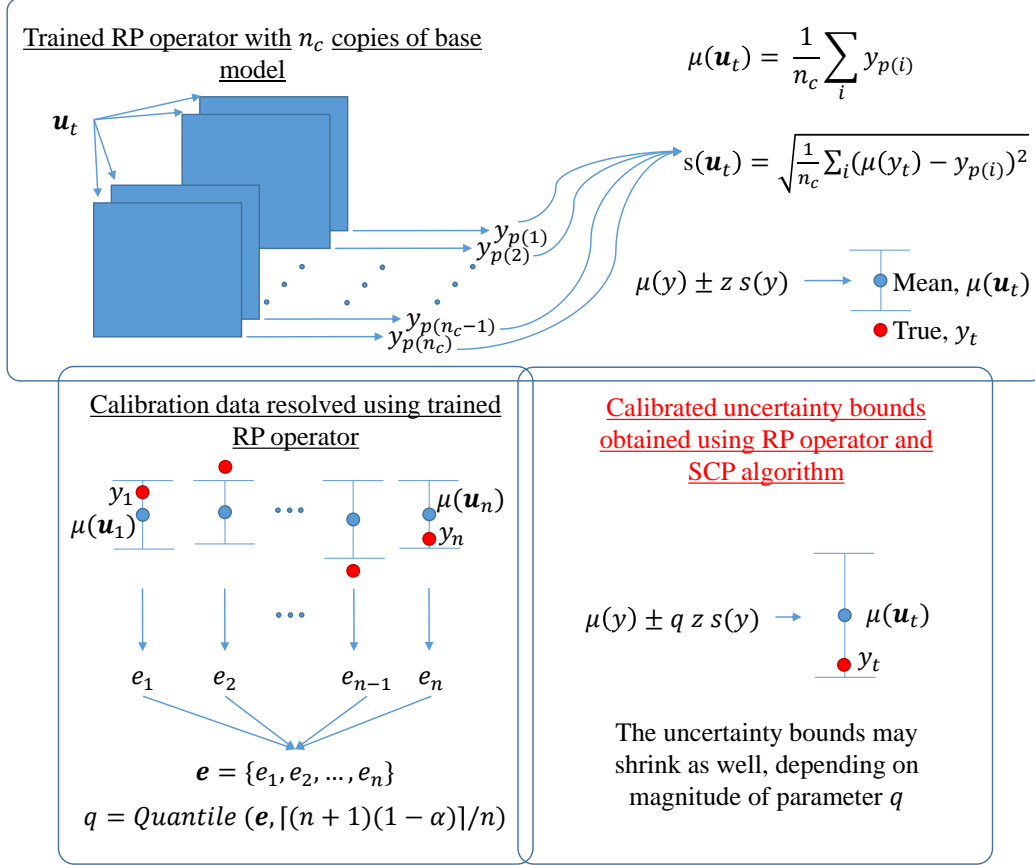


Figure 1: Schematic for the overall framework.

marginal likelihood). Details on training GP is shown in Algorithm 2). Once trained, the predictions at a new location \mathbf{x}^* can be obtained by computing the predictive distribution, $p(q^*|\mathbf{x}^*, \hat{\mathbf{x}}, \mathbf{q})$,

$$p(q^*|\mathbf{x}^*, \hat{\mathbf{x}}, \mathbf{q}) \sim \mathcal{N}(q^*|\mu^*, K^*), \quad (20)$$

where

$$\mu^* = \mathbf{K}(\hat{\mathbf{x}}, \mathbf{x}^*)^\top \mathbf{K}(\hat{\mathbf{x}}, \hat{\mathbf{x}}')^{-1} \mathbf{q} \quad (21)$$

and

$$K^* = K(\mathbf{x}^*, \mathbf{x}^*) - \mathbf{K}(\hat{\mathbf{x}}, \mathbf{x}^*)^\top \mathbf{K}(\hat{\mathbf{x}}, \hat{\mathbf{x}}')^{-1} \mathbf{K}(\hat{\mathbf{x}}, \mathbf{x}^*). \quad (22)$$

Here, $K(\mathbf{x}^*, \mathbf{x}^*) \in \mathbb{R}$, $\mathbf{K}(\hat{\mathbf{x}}, \mathbf{x}^*) \in \mathbb{R}^{n \times 1}$, and $\mathbf{K}(\hat{\mathbf{x}}, \hat{\mathbf{x}}') \in \mathbb{R}^{n \times n}$. Using this procedure, the GP is trained to model the parameter q over the locations \mathbf{x}_{tr_i} on the training grid \mathcal{G}_{tr} and subsequently predict q at the super-resolution grid locations \mathbf{x}_{sr_i} on \mathcal{G}_{sr} . We utilize the predictive mean obtained from GP to obtain the calibrated uncertainty.

One key aspect of GP is selection of covariance kernel. In this work, a rational quadratic function is used as the covariance kernel, and the GP is modeled and trained using the `GaussianProcessRegressor` function from Python's `Scikit-Learn`¹ library.

4 Numerical Illustrations

In this section, we present four examples to illustrate the efficacy of the proposed framework. While the first example deals with the Burger's equation, the second and third examples deal with the two-dimensional Darcy equation defined on a rectangular domain and triangular domain, respectively. As the fourth example, the seismic wave propagation is considered. For all the examples, we present results obtained using both CRP-WNO and CRP-VSWNO models, and

¹https://scikit-learn.org/stable/modules/generated/sklearn.gaussian_process.GaussianProcessRegressor.html

Algorithm 2 Algorithm for training GP.

Require: Training dataset $\{x_{tr_i}, q_i\}_{i=1}^{n_e}$, covariance function $K(\cdot, \cdot; \theta_K)$, initial estimates for θ_K, θ_{K_0} , error threshold ϵ , and an optimizer algorithm.

- 1: $\theta_K \leftarrow \theta_{K_0}, \epsilon' \leftarrow 10 \epsilon$
- 2: **while** $\epsilon' > \epsilon$ **do**
- 3: Compute the negative log-likelihood L_{nll} using training data and parameters θ_K .
- 4: $L_{nll} \propto -\frac{1}{2}(\log |\mathbf{K}| + \mathbf{y}^T \mathbf{K}^{-1} \mathbf{y})$, where \mathbf{y} represents the observation vector.
- 5: Update parameters θ_K using suitable optimizer.
- 6: $\theta_{K_{new}} \leftarrow \theta_K - g\left(\frac{\partial L_{nll}}{\partial \theta_K}\right)$, where $g(\cdot)$ is governed by the choice of optimizer.
- 7: $\theta_{K_{old}} \leftarrow \theta_K$
- 8: $\theta_K \leftarrow \theta_{K_{new}}$
- 9: $\epsilon' = \|\theta_{K_{new}} - \theta_{K_{old}}\|_2^2$
- 10: **end while**

Output: Optimized GP parameters θ_K .

compare the results obtained with those obtained using RP-WNO, RP-VSWNO, Q-WNO, and CRQ-WNO. Additionally, for the fourth example, we also present a comparative assessment between CRP-WNO and RCQNO models.

The first example deals with a dataset generated using the one-dimensional Burgers equation, the second and third examples deal with the two-dimensional Darcy equation defined on a rectangular domain and triangular domain, respectively, and the fourth example deals with a dataset generated using the Helmholtz equation. To learn the datasets in different examples, we use the CRP-WNO and CRP-VSWNO models and compare the results with those obtained when using RP-WNO, RP-VSWNO, Q-WNO, and CRQ-WNO. In the fourth example, we also compare the performance of CRP-WNO against that of RCQNO model. The nomenclature for various deep learning models mentioned above are shown in Table 1. Individual architecture details for WNO based deep learning models in various examples

Table 1: Nomenclature for various deep learning models used in the four examples.

Model	Description
RP-WNO	Randomized Prior Wavelet Neural Operator
CRP-WNO	Conformalized (calibrated) RP-WNO
RP-VSWNO	Randomized Prior Variable Spiking Wavelet Neural Operator
CRP-VSWNO	Conformalized RP-VSWNO
Q-WNO	Quantile Wavelet Neural Operator
CQ-WNO	Conformalized Q-WNO

are given in A. For details on the training of Q-WNO and calibration process of CQ-WNO, refer B. The quantum of training data, calibration data, and the testing data used in various examples is given in Table 2. It should be noted that while we are demonstrating results using only 100 test samples in various examples, trained deep learning models have no such limitation and can be used any number of test samples. For all the examples, we aim to have 95%

Table 2: Dataset size used in various examples.

Example	No. of Samples in Dataset		
	Training	Calibration	Testing
E-I, Burgers Equation	1000	50	100
E-II, Darcy Equation - Rectangular Domain	800	100	100
E-III, Darcy Equation - Triangular Domain	1700	150	100
E-IV, Helmholtz Equation	500	150	100

coverage and hence set $\alpha = 0.05$. The coverage reported in various examples, corresponding to various deep learning models, is based on the observations of the test dataset. Samples from the calibration dataset are not included in coverage results to maintain fairness in comparison. For all the examples, we consider an ensemble size of 10 for the RP

operator networks. Finally, one of the main motivations behind neuroscience inspired operators is to reduce energy consumption. However, the potential of the spiking neurons and its variants such as the variable spiking neurons in energy saving can only be realized while using neuromorphic hardware. In absence of availability of such hardware, a common surrogate metric for energy measurement is the spiking activity [27, 28]. In this study also, we use the same metric to evaluate energy consumption, and report the results obtained in C.

4.1 E-I, Burgers Equation

In the first example, we consider the one-dimensional Burgers equation, which is a nonlinear PDE and is often used in fluid dynamics to model the flow of a viscous fluid. It also finds its application in fields like gas dynamics, nonlinear acoustics, and traffic flow. The Burgers equation is defined as,

$$u_t(x, t) + u(x, t)u_x(x, t) = \nu u_{xx}(x, t), \quad x \in [0, 1], t \in (0, 1], \quad (23)$$

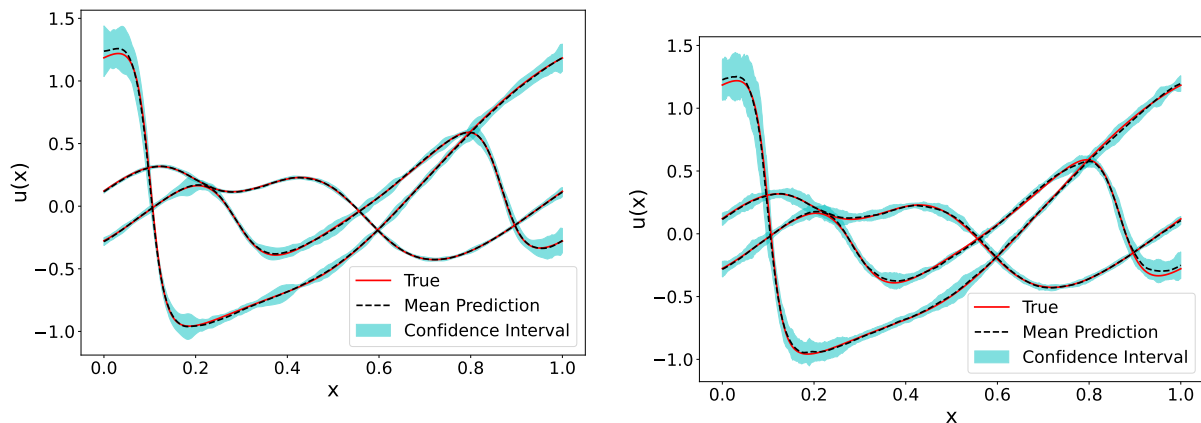
where $\nu = 0.1$ is the viscosity coefficient. Periodic boundary conditions of the form $u(x = 0, t) = u(x = 1, t)$ are considered. Our objective is to learn the operator that maps from initial condition $u(x, 0)$ to the solution at $t = 1$, i.e., $u(x, 1)$,

$$\mathcal{M} : u(x, 0) \mapsto u(x, 1).$$

We assume $u(x, 0)$ to be a Gaussian random field,

$$u(x, 0) \sim N(\mathbf{0}, 625(-\Delta + 25\mathbb{I})^{-2}), \quad (24)$$

where Δ is the Laplacian. For generating data, Eq. (23) is solved using $\Delta t = 1/200$ and by discretizing the spatial domain into 8192 grid points. Once generated, the data is subsampled into a grid with 1024 grid points. For more information on the dataset, readers may follow the source for the dataset, [22].



(a) CRP-WNO, Normalized Mean Square Error (NMSE) = 0.046%.

(b) CRP-VSWNO, NMSE = 0.085%.

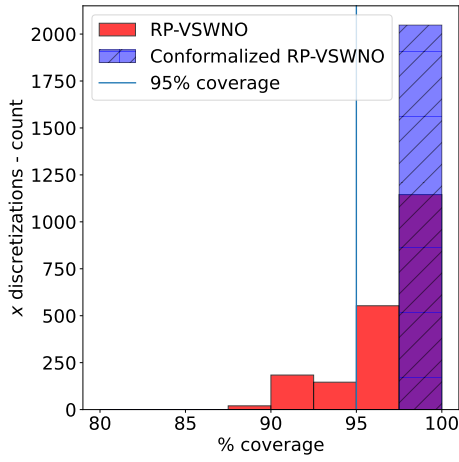
Figure 2: Mean predictions for test inputs obtained using CRP-WNO and CRP-VSWNO compared against the ground truth in E-I. Calibrated confidence intervals obtained using the two networks are also plotted for different test samples.

Fig. 2 shows the mean predictions of CRP-WNO and CRP-VSWNO networks for different test samples and their respective calibrated confidence intervals. The mean predictions closely follow the ground truth, and they are engulfed by the confidence intervals in the regions where they diverge. Table 3 shows the coverage obtained corresponding to various deep learning models. As can be seen that the RP operators give a decent initial measure and the proposed framework utilizing the same RP operator predictions is able to give the desired 95% coverage at all spatial locations. Furthermore, as can be observed, the performance of CQ-WNO is lacking severely compared to the performance of CRP-WNO or CRP-VSWNO. While CQ-WNO is able to give a coverage of $> 95\%$ when average is taken over all spatial locations, when looked at individually, at several locations, its coverage is $< 95\%$. This is not the case with either of the CRP networks.

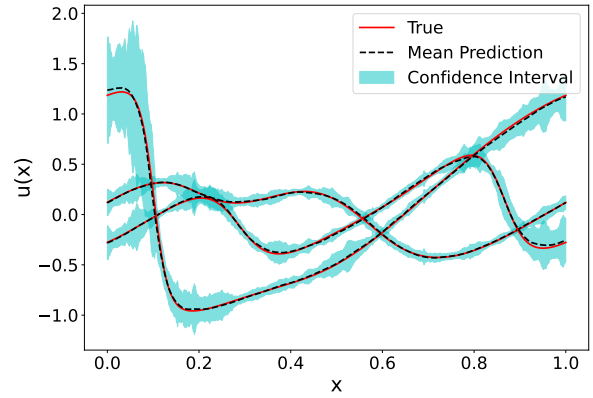
Fig. 3(a) shows the coverage obtained for RP-VSWNO and CRP-VSWNO when predicting outputs at a higher resolution. In the current example, we have trained and calibrated our models for a spatial resolution of 1024. However, for our super-resolution results, we predict outputs corresponding to a spatial resolution of 2048. As can be seen from Fig. 3(a), the coverage improves significantly (as opposed to initial uncertainty estimates obtained from the RP operator)

Table 3: Coverage provided by the confidence intervals generated using various deep learning models and their conformalized versions in E-I. Count for the number of spatial locations where coverage is $< 95\%$ or is $\geq 95\%$ is also included.

Model	Coverage			Count (Out of 1024)	
	Average	Min.	Max.	$< 95\%$	$\geq 95\%$
RP-WNO	94.23	82.00	100.00	422	602
CRP-WNO	99.89	98.00	100.00	0	1024
RP-VSWNO	97.42	92.00	100.00	82	942
CRP-VSWNO	99.66	96.00	100.00	0	1024
Q-WNO	15.83	5.00	25.00	1024	0
CQ-WNO	96.32	89.00	100.00	265	759



(a) Coverage provided by the confidence intervals.



(b) Mean predictions compared against ground truth and confidence intervals obtained using CRP-VSWNO. NMSE = 0.086%.

Figure 3: Super-resolution results for E-I.

despite the original calibration being done on a coarser grid. Fig. 3(b) shows the mean predictions of CRP-VSWNO compared against the ground truth and the corresponding confidence intervals when predicting at the higher resolution of 2048. The mean predictions closely follow the ground truth, and the confidence intervals perform their function well. It should be noted here that the width of confidence intervals obtained when predicting at a higher resolution is more than the width of confidence intervals obtained when predicting at the training resolution. This is because the model is now also predicting at locations that were not considered during training.

4.2 E-II, Darcy Equation on Rectangular Domain

The second example deals with a two-dimensional Darcy flow equation often used in literature to model flow through a porous media,

$$-\nabla(a(x, y)\nabla u(x, y)) = 1, \quad x, y \in (0, 1), \quad (25)$$

where $a(x, y)$ is the permeability and $u(x, y)$ is the pressure. Zero Dirichlet boundary conditions are considered while generating the dataset. The operator to be learned in this example maps the permeability field $a(x, y)$ to the pressure field $u(x, y)$,

$$\mathcal{M} : a(x, y) \mapsto u(x, y). \quad (26)$$

A spatial resolution of 85×85 is considered, resulting in $\delta x = \delta y = 1/85$. The permeability field is assumed to be a Gaussian random field defined as

$$a(x, y) \sim N(\mathbf{0}, (-\Delta + 9\mathbb{I})^{-2}), \quad (27)$$

which is then passed through a mapping function which sets all negative values equal to 3 and all positive values equal to 12. For more details regarding the dataset, refer [22, 23].

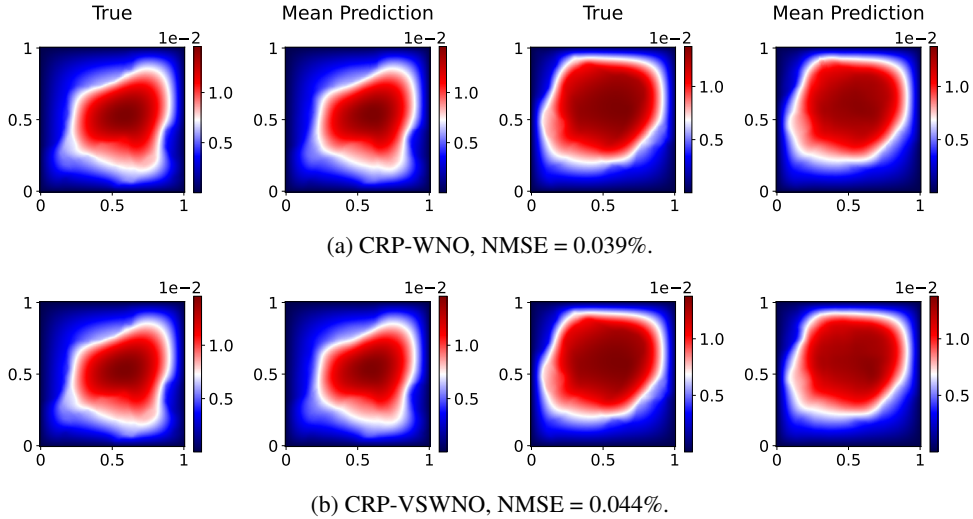


Figure 4: Mean predictions for test inputs obtained using CRP-WNO and CRP-VSWNO compared against the ground truth in E-II.

Fig. 4 shows the mean predictions from CRP-WNO and CRP-VSWNO compared against the ground truth. The mean predictions give a good approximation of the ground truth. Table 4 shows the performance of confidence intervals obtained using various deep learning models. In this example, the performance of RP-WNO and RP-VSWNO

Table 4: Coverage provided by the confidence intervals generated using various deep learning models and their conformalized versions in E-II. Count for the number of discretizations of (x, y) grid where coverage is $< 95\%$ or is $\geq 95\%$ is also included.

Model	Coverage			Count (Out of 7225)	
	Average	Min.	Max.	$< 95\%$	$\geq 95\%$
RP-WNO	72.15	4.00	95.00	7224	1
CRP-WNO	99.49	95.00	100.00	0	7225
RP-VSWNO	83.12	4.00	100.00	6413	812
CRP-VSWNO	99.62	95.00	100.00	0	7225
Q-WNO	51.26	0.00	94.00	7225	0
CQ-WNO	95.07	81.00	100.00	2668	4557

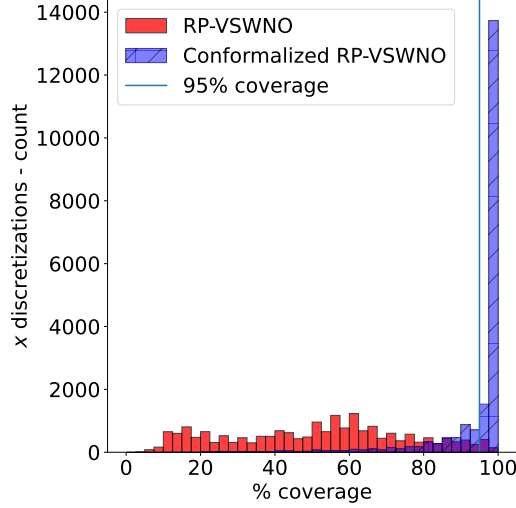
is subpar. However, their conformalized versions, CRP-WNO and CRP-VSWNO, give the expected coverage of $\geq 95\%$ at all locations of the (x, y) grid. Furthermore, the performance of CQ-WNO is worse than that of both the conformalized RP operators. Similar to the previous example, although CQ-WNO reaches the 95% mark in the average sense, it fails to provide adequate coverage at several locations of (x, y) grid.

Figure 5 illustrates the super-resolution results using RP-VSWNO as the base model. The training and calibration grid resolution was set to 85×85 , while the prediction grid resolution was increased to 141×141 . During calibration, the parameter $\mathbf{q} \in \mathbb{R}^{85 \times 85}$ was computed and mapped to the 85×85 grid using a Gaussian process. Subsequently, \mathbf{q} was predicted for the refined 141×141 grid. Figure 5(a) demonstrates that the confidence intervals for super-resolution predictions improve significantly, as opposed to randomized prior operator, when employing CRP-VSWNO. Figure 5(b) compares the predictions from CRP-VSWNO against the ground truth for the higher resolution grid. The results indicate that the model provides a reasonable approximation of the ground truth.

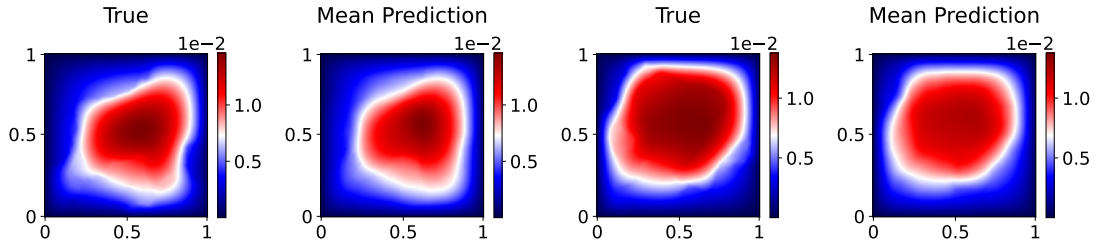
4.3 E-III, Darcy on Triangular Domain with a Notch

This example again deals with a two dimensional Darcy equation, defined as,

$$-\nabla(0.1 \nabla u(x, y)) = -1, \quad x, y \in [0, 1]. \tag{28}$$



(a) Coverage provided by the confidence intervals.



(b) Mean predictions obtained using RP-VSWNO compared against ground truth. NMSE = 0.849%.

Figure 5: Super-resolution results for E-II.

However, the equation is now defined on a triangular domain Ω with a rectangular notch. The boundary condition $u(x, y)|_{\partial\Omega}$ is assumed to be random, and sampled from a Gaussian random field,

$$u(\mathbf{x}) = GP(0, K(\mathbf{x}, \mathbf{x}')),$$

$$K(\mathbf{x}, \mathbf{x}') = \exp\left(-\frac{1}{2l^2}(\mathbf{x} - \mathbf{x}')^T(\mathbf{x} - \mathbf{x}')\right), \quad l = 0.2, \quad \mathbf{x}, \mathbf{x}' \in [0, 1]^2, \quad (29)$$

where \mathbf{x} and \mathbf{x}' represent different grid points on the boundary. In this example, the objective is to learn the operator that maps the boundary conditions to the solution $u(x, y)$,

$$\mathcal{M} : u(x, y)|_{\partial\Omega} \mapsto u(x, y) \quad (30)$$

For further details, interested readers can refer [46].

Results shown in Fig. 6 and Table 5 reinforce the trends observed in previous examples. CRP-WNO and CRP-VSWNO are able to give expected coverage, and at the same time, the mean predictions obtained closely follow the ground truth.

4.4 E-IV, Helmholtz Equation

The fourth example deals with the Helmholtz equation, which is a time-independent form of the wave equation, and is often used to study the effect of traveling waves in areas like seismic ground exploration, radiation studies, etc. The governing equation in this case is defined as follows,

$$\nabla^2 u(x, z; \omega) + \frac{\omega^2}{\nu(x, z)^2} u(x, z; \omega) = f(x_s, z_s; \omega), \quad x, z \in [0, 690], \quad \delta x, \delta z = 70 \quad (31)$$

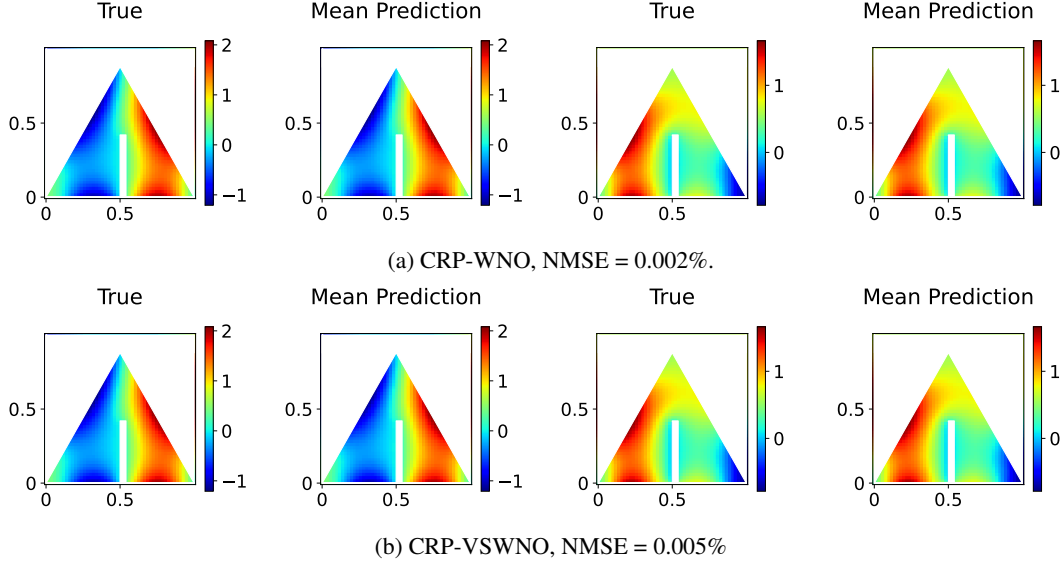


Figure 6: Mean predictions for test inputs obtained using CRP-WNO and CRP-VSWNO compared against the ground truth in E-III.

Table 5: Coverage provided by the confidence intervals generated using various deep learning models and their conformalized versions in E-III. Count for the number of discretizations of (x, y) grid where coverage is $< 95\%$ or $\geq 95\%$ is also included.

Model	Coverage			Count (Out of 1102)	
	Average	Min.	Max.	$< 95\%$	$\geq 95\%$
RP-WNO	94.89	0.00	100.00	141	961
CRP-WNO	99.70	95.00	100.00	0	1102
RP-VSWNO	97.18	2.00	100.00	59	1043
CRP-VSWNO	99.75	97.00	100.00	0	1102
Q-WNO	21.20	0.00	66.00	1102	0
CQ-WNO	94.33	82.00	100.00	515	587

where $u(x, z; \omega)$ is the magnitude of frequency domain pressure wavefield, corresponding to angular frequency ω at location (x, z) . (x_s, z_s) are the coordinates of the point source, $\nu(x, z)$ is the velocity at location (x, z) . While generating the dataset, the Helmholtz equation is not solved directly; rather, the two-dimensional wave equation is solved first in the time domain, and then the solution is converted to the frequency domain to obtain the solution of the Helmholtz equation. The wave equation is defined as,

$$\nabla^2 p(x, z, t) - \frac{1}{\nu(x, z)^2} \frac{\partial^2 p(x, z, t)}{\partial t^2} = s(x_s, z_s, t), \quad (32)$$

where $p(x, z, t)$ is the pressure wavefield and $s(x_s, z_s, t)$ is the point source located at (x_s, z_s) . While solving, the values for various parameters are considered as follows: $x_s = 680$, $z_s = 10$, and $s(x_s, z_s, t) = 1$. Mur's absorbing boundary conditions are considered, and a spatial resolution of 70×70 is considered. The velocity of the wave over the domain creates a distinction between different samples of the dataset, and the various velocity maps used are taken from the OpenFWI datasets² [47].

The Helmholtz equation can be solved across a wide range of frequencies, but lower frequencies typically dominate the solution's behavior. In this example, we focus on frequencies ≤ 10 Hz, specifically 1 Hz, 3 Hz, 5 Hz, 7 Hz, and 9 Hz. The model maps the input, comprising angular frequency information and the velocity field $\nu(x, z)$, to the corresponding output $u(x, z; \omega)$,

$$\mathcal{M} : \nu(x, z) \mapsto u(x, z; \omega), \quad (33)$$

²<https://openfwi-lanl.github.io/docs/data.html>, accessed on 12-11-2024, FlatVela dataset

where the output $u(x, z; \omega)$ consists of both real and imaginary components, necessitating the use of two separate models to capture the complete solution. We provide frequency information as input to the network, and hence, a single neural operator can capture the response corresponding to all frequencies. Given the complexity of this problem, we consider 20 copies for the randomized prior network and select the best 10.

Table 6: Percentage NMSE values observed in CRP-WNO and CRP-VSWNO networks of E-IV, when comparing network’s mean predictions with ground truth.

Network	Component	Frequency				
		1Hz	3Hz	5Hz	7Hz	9Hz
CRP-WNO	Real	0.024	0.024	0.075	0.184	0.519
	Imaginary	0.002	0.002	0.004	0.006	0.011
CRP-VSWNO	Real	0.047	0.069	0.232	0.615	1.297
	Imaginary	0.004	0.008	0.011	0.018	0.029

Table 6 shows the NMSE values obtained when comparing the mean predictions obtained using CRP-WNO and CRP-VSWNO models against the corresponding ground truth. As can be seen, the error observed is marginal, and the mean predictions are a good approximation of the ground truth. Fig. 7 compares the mean prediction of CRP-VSWNO the ground truth corresponding to one test input. Both real and imaginary components corresponding to 1Hz and 9Hz frequencies are plotted. As can be seen, the mean prediction closely follows the ground truth. Table 7 shows the number of discretizations where coverage is $< 95\%$ or $\geq 95\%$ when using RP-WNO, RP-VSWNO, Q-WNO or their conformalized variants. It should be noted that although during the training of various deep learning models, the dataset contained information corresponding to all the frequencies, during calibration, outputs corresponding to different frequencies were calibrated individually. This is done to show the flexibility of the adopted approach. The results show that barring a single grid location, the expected coverage of $\geq 95\%$ is achieved at almost all locations when using CRP-WNO or CRP-VSWNO, whereas other deep learning models fail to achieve the same.

As an additional case study, Table 8 illustrates the performance of CRP-WNO as compared to RCQNO. The results obtained for RCQNO are based on the code implementation given in the GitHub^{3,4} repository. As can be seen from the table, CRP-WNO has produced tighter bounds, and the NMSE observed is also lower for the CRP-WNO network. The RCQNO framework failed to provide the required coverage when predicting imaginary component corresponding to 1Hz and 3Hz frequencies at one and 45 grid locations respectively. On the contrary, the CRP-WNO failed to provide the coverage at a single grid location only, when predicting imaginary component corresponding to 3Hz frequency.

5 Conclusion

The estimates for the uncertainty associated with the neural operator predictions give users auxiliary confidence when undertaking decision-making tasks. These estimates become especially essential for the spiking variants of these operators as they exhibit sparse communication to conserve energy, which can potentially lead to reduced accuracy in predictions. To address this, we propose in this paper, a distribution free uncertainty quantification framework in neuroscience inspired spiking operators. The proposed framework uses the uncertainty bounds from randomized prior (RP) operators as its initial uncertainty estimates and calibrates them using the split conformal prediction (SCP) algorithm to provide the required coverage. The selection of the RP operator for obtaining the initial estimate of uncertainty is based on the hypothesis that a good initial estimate will improve the SCP algorithm’s calibration performance. It is also based on the fact that the RP operators are easily scalable to complex architectures, are computationally efficient, and can account for prior information while being set in a deterministic framework.

Super-resolution is a defining property for operator learning algorithms, and gauging uncertainty associated with super-resolution predictions is important because, in this case, the trained model is predicting at solution grid locations that are unseen during training. The conventional SCP framework, unfortunately, is not designed for zero-shot super-resolution. In response to this challenge, we also enhance the algorithm to allow uncertainty quantification in zero-shot super-resolution setup. The developed algorithm is integrated with the recently developed variable spiking wavelet neural operator (VSWNO) and the vanilla wavelet neural operator (WNO) so as to enable uncertainty quantification in these operators. The resulting algorithms are referred to as CRP-VSWNO and CRP-WNO.

³<https://github.com/ziqui-ma/neuraloperator/tree/ziqui/uq/uq>, accessed on: 04 November 2024

⁴https://github.com/ziqui-ma/neuraloperator/blob/ziqui/uq/uq/FNO_darcy_residual.py, accessed on: 04 November 2024

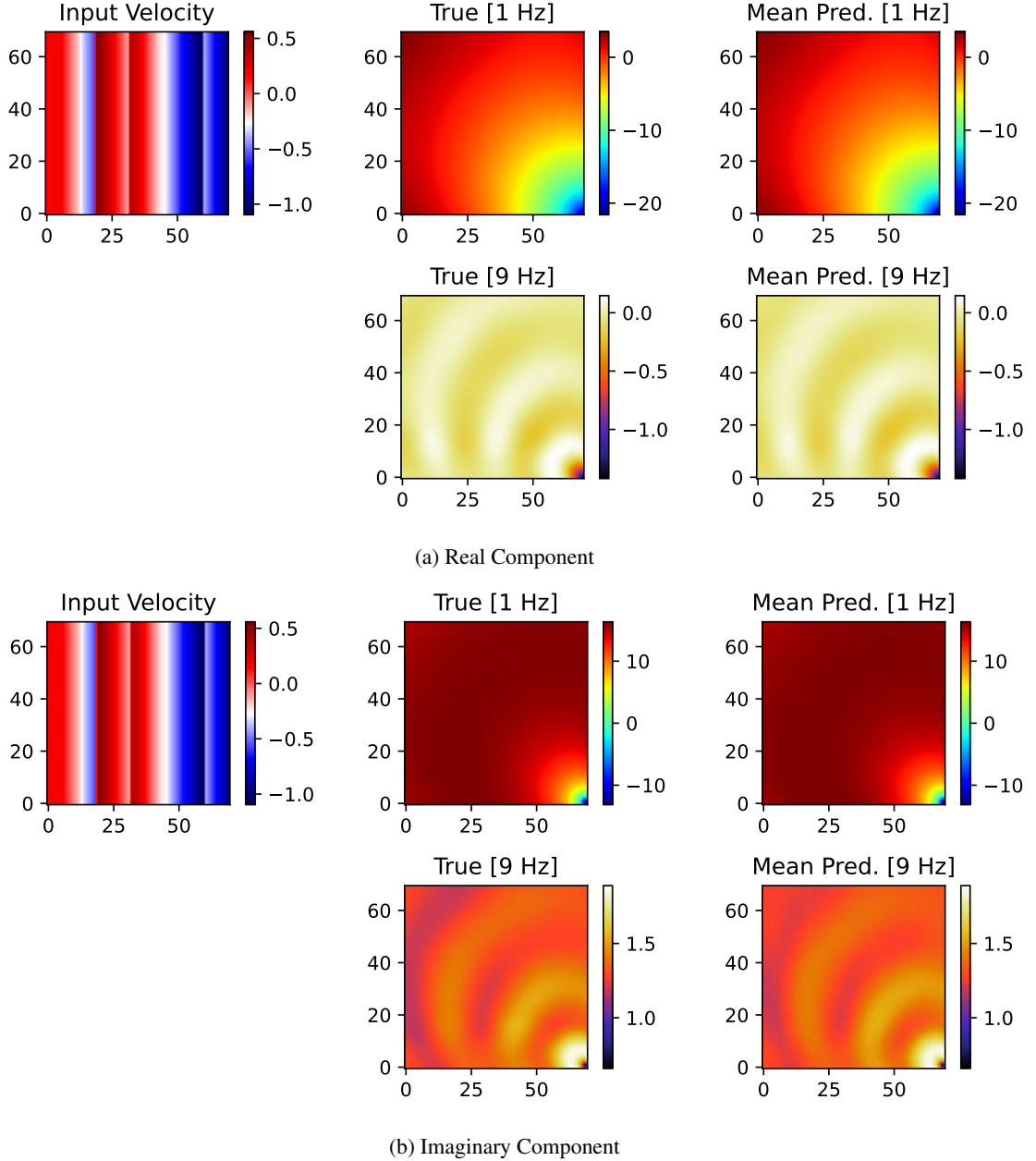


Figure 7: Mean predictions corresponding to one test input obtained using CRP-VSWNO compared against the ground truth in E-IV.

To test the validity of the proposed framework, we show four examples covering both one-dimensional and two-dimensional partial differential equations. VSWNO and vanilla WNO are used as our base operator learning algorithms. The key findings of the paper are as follows,

- With the exception of example example four, where the coverage criterion is not satisfied at one of the location of the solution grid, the CRP-WNO and the CRP-VSWNO are able to give the required coverage at all locations of the solution grid when tested across other examples. On the contrary, the conformalized quantile variant fails to yield desired coverage at several locations. This establishes the importance of initial uncertainty estimates as hypothesized in this work.

Table 7: Count for the number of discretizations of (x, y) grid where coverage is $<95\%$ or is $\geq 95\%$ obtained using various deep learning models and their conformalized versions in E-IV.(a) Results corresponding to $\omega = 1\text{Hz}$.

Model			RP-WNO	CRP-WNO	RP-VSWNO	CRP-VSWNO	Q-WNO	CQ-WNO
Count (out of 4900)	$< 95\%$	Real	2589	0	2496	0	4900	3594
		Imaginary	2644	0	2858	0	4697	1705
	$\geq 95\%$	Real	2311	4900	2404	4900	0	1306
		Imaginary	2256	4900	2042	4900	203	3195

(b) Results corresponding to $\omega = 3\text{Hz}$.

Model			RP-WNO	CRP-WNO	RP-VSWNO	CRP-VSWNO	Q-WNO	CQ-WNO
Count (out of 4900)	$< 95\%$	Real	1330	0	958	0	4900	3132
		Imaginary	1950	1	2528	0	4897	3016
	$\geq 95\%$	Real	3570	4900	3942	4900	0	1768
		Imaginary	2950	4899	2372	4900	3	1884

(c) Results corresponding to $\omega = 5\text{Hz}$.

Model			RP-WNO	CRP-WNO	RP-VSWNO	CRP-VSWNO	Q-WNO	CQ-WNO
Count (out of 4900)	$< 95\%$	Real	2700	0	699	0	4900	1746
		Imaginary	2943	0	2174	0	4897	1906
	$\geq 95\%$	Real	2200	4900	4201	4900	0	3154
		Imaginary	1957	4900	2726	4900	3	2994

(d) Results corresponding to $\omega = 7\text{Hz}$.

Model			RP-WNO	CRP-WNO	RP-VSWNO	CRP-VSWNO	Q-WNO	CQ-WNO
Count (out of 4900)	$< 95\%$	Real	3544	0	1097	0	4900	1877
		Imaginary	3243	0	2627	0	4900	1731
	$\geq 95\%$	Real	1356	4900	3803	4900	0	3023
		Imaginary	1657	4900	2273	4900	0	3169

(e) Results corresponding to $\omega = 9\text{Hz}$.

Model			RP-WNO	CRP-WNO	RP-VSWNO	CRP-VSWNO	Q-WNO	CQ-WNO
Count (out of 4900)	$< 95\%$	Real	4382	0	1196	0	4900	1805
		Imaginary	3413	0	2755	0	4898	1874
	$\geq 95\%$	Real	518	4900	3704	4900	0	3095
		Imaginary	1487	4900	2145	4900	2	3026

- As illustrated in the first two example, the proposed approach yield excellent results in the zero-shot super-resolution scenario as well. This illustrates that the efficacy of the proposed zero-shot super-resolution enabled split conformal algorithm.
- In the fourth example, we also compare the results obtained using the proposed framework with those obtained using the risk controlling quantile neural operator. While both the frameworks were yield desired coverage on average (over all locations of the solution grid), the proposed approach yield tighter bounds, and its mean prediction gave a better reflection of the ground truth. Also, unlike the proposed approach, which produces a separate conformal parameter for all locations of the solution grid, the RCQNO framework produces a single conformal parameter for the whole domain, leading to a possible overestimation of uncertainty at some locations on the output domain.

Overall, the proposed framework benefits from the good initial predictions of the RP operators, and subsequently, the SCP can calibrate them with a meager dataset. The GP also aids in improving the uncertainty estimates compared to the initial RP-operator estimates in a super-resolution setting. To further extend the literature on the discussed framework,

Table 8: Comparison between the performance of RCQNO and CRP-WNO. Since, the average coverage obtained is $\geq 95\%$ in both approaches, we compare using the average width of the calibrated confidence interval d and the percentage NMSE values obtained when comparing predictions against the ground truth. n here represents the quantum of calibration data used.

Component	Frequency	RCQNO			CRP-WNO		
		n	$d(\times 10^{-2})$	% NMSE	n	$d(\times 10^{-2})$	% NMSE
Real	1Hz		48.88	0.023		33.75	0.024
	3Hz		22.64	0.204		6.36	0.024
	5Hz	500	22.59	0.910	150	4.97	0.075
	7Hz		22.28	2.482		4.67	0.184
	9Hz		23.37	4.178		5.15	0.519
Imaginary	1Hz		122.73	0.013		51.89	0.002
	3Hz		53.94	0.023		15.21	0.002
	5Hz	500	44.51	0.027	150	13.01	0.004
	7Hz		38.01	0.041		12.27	0.006
	9Hz		34.16	0.060		11.96	0.011

studies concerning the optimum size of the calibration dataset may be carried out. Furthermore, a comprehensive empirical study showing whether the conditional coverage is obtained when using the discussed framework may also be carried out.

Acknowledgment

SG acknowledges the financial support received from the Ministry of Education, India, in the form of the Prime Minister’s Research Fellows (PMRF) scholarship. SC acknowledges the financial support received from Anusandhan National Research Foundation (ANRF) via grant no. CRG/2023/007667 and from the Ministry of Port and Shipping via letter no. ST-14011/74/MT (356529).

References

- [1] Michael I Jordan and Tom M Mitchell. Machine learning: Trends, perspectives, and prospects. *Science*, 349(6245):255–260, 2015.
- [2] Batta Mahesh. Machine learning algorithms-a review. *International Journal of Science and Research (IJSR).[Internet]*, 9(1):381–386, 2020.
- [3] Ethem Alpaydin. *Machine learning*. MIT press, 2021.
- [4] Vincent Dubourg, Bruno Sudret, and Jean-Marc Bourinet. Reliability-based design optimization using kriging surrogates and subset simulation. *Structural and Multidisciplinary Optimization*, 44:673–690, 2011.
- [5] Atin Roy and Subrata Chakraborty. Support vector machine in structural reliability analysis: A review. *Reliability Engineering & System Safety*, 233:109126, 2023.
- [6] Axay Thapa, Atin Roy, and Subrata Chakraborty. Reliability analyses of underground tunnels by an adaptive support vector regression model. *Computers and Geotechnics*, 172:106418, 2024.
- [7] Kazuma Kobayashi and Syed Bahauddin Alam. Explainable, interpretable, and trustworthy ai for an intelligent digital twin: A case study on remaining useful life. *Engineering Applications of Artificial Intelligence*, 129:107620, 2024.
- [8] Kazuma Kobayashi and Syed Bahauddin Alam. Deep neural operator-driven real-time inference to enable digital twin solutions for nuclear energy systems. *Scientific reports*, 14(1):2101, 2024.
- [9] Aanchna Sharma, Tanmoy Mukhopadhyay, Sanjay Mavinkere Rangappa, Suchart Siengchin, and Vinod Kushvaha. Advances in computational intelligence of polymer composite materials: machine learning assisted modeling, analysis and design. *Archives of Computational Methods in Engineering*, 29(5):3341–3385, 2022.
- [10] Shailesh Garg, Ankush Gogoi, Souvik Chakraborty, and Budhaditya Hazra. Machine learning based digital twin for stochastic nonlinear multi-degree of freedom dynamical system. *Probabilistic Engineering Mechanics*, 66:103173, 2021.

- [11] Jinshuai Bai, Zhongya Lin, Yizheng Wang, Jiancong Wen, Yinghua Liu, Timon Rabczuk, YuanTong Gu, and Xi-Qiao Feng. Energy-based physics-informed neural network for frictionless contact problems under large deformation. *arXiv preprint arXiv:2411.03671*, 2024.
- [12] Yizheng Wang, Jinshuai Bai, Zhongya Lin, Qimin Wang, Cosmin Anitescu, Jia Sun, Mohammad Sadegh Es-haghi, Yuantong Gu, Xi-Qiao Feng, Xiaoying Zhuang, et al. Artificial intelligence for partial differential equations in computational mechanics: A review. *arXiv preprint arXiv:2410.19843*, 2024.
- [13] Kiran Bhaganagar, Prasanna Kolar, Syed Hasib Akhter Faruqui, Diganta Bhattacharjee, Adel Alaeddini, and Kamesh Subbarao. A novel machine-learning framework with a moving platform for maritime drift calculations. *Frontiers in Marine Science*, 9:831501, 2022.
- [14] Kiran Bhaganagar and David Chambers. Accelerated neural network solvers of navier stokes equations for turbulent flows. *Bulletin of the American Physical Society*, 2024.
- [15] Salvatore Cuomo, Vincenzo Schiano Di Cola, Fabio Giampaolo, Gianluigi Rozza, Maziar Raissi, and Francesco Piccialli. Scientific machine learning through physics-informed neural networks: Where we are and what’s next. *Journal of Scientific Computing*, 92(3):88, 2022.
- [16] Jeyan Thiyagalingam, Mallikarjun Shankar, Geoffrey Fox, and Tony Hey. Scientific machine learning benchmarks. *Nature Reviews Physics*, 4(6):413–420, 2022.
- [17] Tony Hey, Keith Butler, Sam Jackson, and Jeyarajan Thiyagalingam. Machine learning and big scientific data. *Philosophical Transactions of the Royal Society A*, 378(2166):20190054, 2020.
- [18] Kevin Gurney. *An introduction to neural networks*. CRC press, 2018.
- [19] Yann LeCun, Yoshua Bengio, and Geoffrey Hinton. Deep learning. *nature*, 521(7553):436–444, 2015.
- [20] Oludare Isaac Abiodun, Aman Jantan, Abiodun Esther Omolara, Kemi Victoria Dada, Nachaat AbdElatif Mohamed, and Humaira Arshad. State-of-the-art in artificial neural network applications: A survey. *Heliyon*, 4(11), 2018.
- [21] Lu Lu, Pengzhan Jin, Guofei Pang, Zhongqiang Zhang, and George Em Karniadakis. Learning nonlinear operators via deepnet based on the universal approximation theorem of operators. *Nature machine intelligence*, 3(3):218–229, 2021.
- [22] Zongyi Li, Nikola Kovachki, Kamyar Azizzadenesheli, Burigede Liu, Kaushik Bhattacharya, Andrew Stuart, and Anima Anandkumar. Fourier neural operator for parametric partial differential equations. *arXiv preprint arXiv:2010.08895*, 2020.
- [23] Tapas Tripura and Souvik Chakraborty. Wavelet neural operator for solving parametric partial differential equations in computational mechanics problems. *Computer Methods in Applied Mechanics and Engineering*, 404:115783, 2023.
- [24] Nikola Kovachki, Zongyi Li, Burigede Liu, Kamyar Azizzadenesheli, Kaushik Bhattacharya, Andrew Stuart, and Anima Anandkumar. Neural operator: Learning maps between function spaces with applications to pdes. *Journal of Machine Learning Research*, 24(89):1–97, 2023.
- [25] Carlos A Felippa. Introduction to finite element methods. *University of Colorado*, 885, 2004.
- [26] Singiresu S Rao. *The finite element method in engineering*. Elsevier, 2010.
- [27] Shailesh Garg and Souvik Chakraborty. Neuroscience inspired neural operator for partial differential equations. *Journal of Computational Physics*, 515:113266, 2024.
- [28] Adar Kahana, Qian Zhang, Leonard Gleyzer, and George Em Karniadakis. Spiking neural operators for scientific machine learning. *arXiv preprint arXiv:2205.10130*, 2022.
- [29] Anastasios N Angelopoulos, Stephen Bates, et al. Conformal prediction: A gentle introduction. *Foundations and Trends® in Machine Learning*, 16(4):494–591, 2023.
- [30] Jing Lei, Max G’Sell, Alessandro Rinaldo, Ryan J Tibshirani, and Larry Wasserman. Distribution-free predictive inference for regression. *Journal of the American Statistical Association*, 113(523):1094–1111, 2018.
- [31] Christian Moya, Amirhossein Mollaali, Zecheng Zhang, Lu Lu, and Guang Lin. Conformalized-deepnet: A distribution-free framework for uncertainty quantification in deep operator networks. *arXiv preprint arXiv:2402.15406*, 2024.
- [32] Ziqi Ma, Kamyar Azizzadenesheli, and Anima Anandkumar. Calibrated uncertainty quantification for operator learning via conformal prediction. *arXiv preprint arXiv:2402.01960*, 2024.

- [33] Laurent Valentin Jospin, Hamid Laga, Farid Boussaid, Wray Buntine, and Mohammed Bannamoun. Hands-on bayesian neural networks—a tutorial for deep learning users. *IEEE Computational Intelligence Magazine*, 17(2):29–48, 2022.
- [34] Pavel Izmailov, Sharad Vikram, Matthew D Hoffman, and Andrew Gordon Gordon Wilson. What are bayesian neural network posteriors really like? In *International conference on machine learning*, pages 4629–4640. PMLR, 2021.
- [35] Charles Blundell, Julien Cornebise, Koray Kavukcuoglu, and Daan Wierstra. Weight uncertainty in neural network. In *International conference on machine learning*, pages 1613–1622. PMLR, 2015.
- [36] Glenn Shafer and Vladimir Vovk. A tutorial on conformal prediction. *Journal of Machine Learning Research*, 9(3), 2008.
- [37] Ian Osband, John Aslanides, and Albin Cassirer. Randomized prior functions for deep reinforcement learning. *Advances in Neural Information Processing Systems*, 31, 2018.
- [38] Shailesh Garg and Souvik Chakraborty. Randomized prior wavelet neural operator for uncertainty quantification. *arXiv preprint arXiv:2302.01051*, 2023.
- [39] Christopher KI Williams and Carl Edward Rasmussen. *Gaussian processes for machine learning*, volume 2. MIT press Cambridge, MA, 2006.
- [40] Eric Schulz, Maarten Speekenbrink, and Andreas Krause. A tutorial on gaussian process regression: Modelling, exploring, and exploiting functions. *Journal of mathematical psychology*, 85:1–16, 2018.
- [41] Lingxin Hao and Daniel Q Naiman. *Quantile regression*. Number 149. Sage, 2007.
- [42] Roger Koenker and Kevin F Hallock. Quantile regression. *Journal of economic perspectives*, 15(4):143–156, 2001.
- [43] Shailesh Garg and Souvik Chakraborty. Neuroscience inspired scientific machine learning (part-1): Variable spiking neuron for regression. *arXiv preprint arXiv:2311.09267*, 2023.
- [44] Emre O Neftci, Hesham Mostafa, and Friedemann Zenke. Surrogate gradient learning in spiking neural networks: Bringing the power of gradient-based optimization to spiking neural networks. *IEEE Signal Processing Magazine*, 36(6):51–63, 2019.
- [45] Souvik Chakraborty and Rajib Chowdhury. Graph-theoretic-approach-assisted gaussian process for nonlinear stochastic dynamic analysis under generalized loading. *Journal of Engineering Mechanics*, 145(12):04019105, 2019.
- [46] Lu Lu, Xuhui Meng, Shengze Cai, Zhiping Mao, Somdatta Goswami, Zhongqiang Zhang, and George Em Karniadakis. A comprehensive and fair comparison of two neural operators (with practical extensions) based on fair data. *Computer Methods in Applied Mechanics and Engineering*, 393:114778, 2022.
- [47] Chengyuan Deng, Shihang Feng, Hanchen Wang, Xitong Zhang, Peng Jin, Yanan Feng, Qili Zeng, Yinpeng Chen, and Youzuo Lin. Openfwi: Large-scale multi-structural benchmark datasets for full waveform inversion. *Advances in Neural Information Processing Systems*, 35:6007–6020, 2022.

A Wavelet Neural Operator and the Architecture Details

In this section, we discuss the architecture of WNO based deep learning models used in various examples. But before delving into its architecture, let us first discuss the theory behind theory behind neural operators and WNO. Neural operators are a class of deep learning architecture that aims to learn some operator $\mathcal{O}_P : \mathcal{I} \rightarrow \mathcal{O}$, that maps the input function space \mathcal{I} to the output function space \mathcal{O} . To achieve this, a parametric map \mathcal{G}_ϕ is formed that is described as follows,

$$\mathcal{O}_P \simeq \mathcal{G}_\phi = \mathcal{P} \circ \sigma(\mathcal{W}_L + \mathcal{K}_L + b_L) \circ \cdots \circ \sigma(\mathcal{W}_1 + \mathcal{K}_1 + b_1) \circ \mathcal{U}, \quad (34)$$

where \mathcal{P} is the projecting operator, \mathcal{U} is the uplifting operator, \mathcal{W}_i is a local operator, \mathcal{K}_i is a kernel integral operator and b_i is a bias function. The operators \mathcal{U} and \mathcal{P} are usually represented in neural operators by a simple neural network, and \mathcal{W}_i is usually represented by a pointwise neural network, generally a convolution layer. $\sigma(\cdot)$ represents a continuous activation and the operation $\sigma(\mathcal{W}_i + \mathcal{K}_i + b_i)$ is repeated for L layers. The definition of the integral operator \mathcal{K}_i is unique to the specific operator learning algorithm in consideration. In WNO, for an arbitrary function v_i with domain \mathcal{D} , which is input to the i^{th} intermediary layer, the operator \mathcal{K}_i is defined as,

$$\mathcal{K}_i v_i(x) = W^{-1}(R_i W(v_i))(x), \quad x \in \mathcal{D}, \quad (35)$$

where $W(\cdot)$ and $W^{-1}(\cdot)$ represent the wavelet and inverse wavelet transform respectively and R_i is a parameterized kernel. The wavelet and inverse wavelet transform operations on a function $f : \mathcal{D} \rightarrow \mathbb{R}^{d_f}$ is defined as,

$$\begin{aligned} W(f)(x) &= f_w(\gamma, \beta) = \int_{\mathcal{D}} f(x) \frac{1}{|\gamma|^{1/2}} \psi\left(\frac{x-\beta}{\gamma}\right) dx, \\ W^{-1}(f_w)(\gamma, \beta) &= f(x) = \frac{1}{C_\psi} \int_0^\infty \int_{\mathcal{D}} f_w(\gamma, \beta) \frac{1}{|\gamma|^{1/2}} \tilde{\psi}\left(\frac{x-\beta}{\gamma}\right) d\beta \frac{d\gamma}{\gamma^2}, \\ C_\psi &= 2\pi \int_{\mathcal{D}} \frac{|\psi_w|^2}{w} \end{aligned} \quad (36)$$

where $\gamma \in \mathbb{R}^+$ and $\beta \in \mathbb{R}$ are the scaling and translation parameters respectively. $\psi(\cdot)$ is an orthonormal mother wavelet and $\tilde{\psi}(\cdot)$ is its dual function. ψ_w represents the Fourier transform of the mother wavelet ψ . For more details regarding WNO architecture, readers are advised to follow [23].

The model selection and hyperparameter selection for WNO models in various examples were done based on random search optimization and experience from working on WNO architecture. ADAM optimizer was used to optimize various deep learning models, and the learning rate was taken to be equal to 0.001. L^2 error was used to train the RP-WNO and RP-VSWNO networks. In RP-VSWNO networks, the spiking activity of VSNs was also penalized using SLF. The projecting operator \mathcal{P} and uplifting operator \mathcal{U} are modeled using two-layered and single-layered neural networks. In the neural network representing the projecting operator, the final layer has a single node in all the examples. The remaining details regarding network architecture are given in Table 9. GeLU activation is used between

Table 9: Network architecture details in various examples. CWT refers to Continuous Wavelet Transform and DWT refers to Discrete Wavelet Transform. L refers to the number of iterative layers (refer (35)) used, and m refers to the number of wavelet decompositions carried out in each iterative layer.

Example	Nodes in first layer		L	Wavelet	m
	\mathcal{P}	\mathcal{U}			
E-I, Burgers Equation	128	64	4	DWT - db6	8
E-II, Darcy Equation on Rectangular Domain	128	64	4	DWT - db4	4
E-III, Darcy Equation on Triangular Domain	128	64	4	DWT - db6	3
E-IV, Helmholtz Equation - Real Component	64	64	4	CWT	4

two iterative layers and between two layers of the network representing the projecting operator \mathcal{P} . Inputs and outputs are normalized in E-II to E-IV. In the prior network of the RP networks, all other details are kept the same, except the number of iterative layers is reduced to two. In VS-WNO networks, the continuous activations are replaced by VSNs in the trainable network of RP setup. Any other miscellaneous details can be referred from the sample codes provided in the GitHub repository (to be released after acceptance).

B Q-WNO and CQ-WNO

The Quantile WNO or Q-WNO, as referenced in the text, is a variant of vanilla WNO, which is trained using the concepts of quantile regression [31, 41, 42]. The idea here is to train two separate models, one corresponding to $\alpha/2$ quantile and the other corresponding to $1 - \alpha/2$ quantile. The respective predictions obtained combined should, in theory, give coverage such that the true outputs lie between the two predictions with probability $\geq (1 - \alpha)$. Now to train the vanilla WNO network corresponding to η quantile, the loss function L is defined as follows,

$$L = \begin{cases} \eta \|\mathbf{y} - \tilde{\mathbf{y}}\|, & \text{if } \|\mathbf{y}\| \geq \|\tilde{\mathbf{y}}\| \\ (1 - \eta) \|\mathbf{y} - \tilde{\mathbf{y}}\|, & \text{if } \|\mathbf{y}\| < \|\tilde{\mathbf{y}}\| \end{cases}, \quad (37)$$

where \mathbf{y} is the true solution and $\tilde{\mathbf{y}}$ is the corresponding prediction. Now, let $\tilde{\mathbf{y}}_1$ be the prediction corresponding to the network trained for $\eta = \alpha/2$ and $\tilde{\mathbf{y}}_2$ be the prediction corresponding to the network trained for $\eta = 1 - \alpha/2$. The initial confidence interval can thus be defined as,

$$\mathcal{C}_{ini} = [\tilde{\mathbf{y}}_1, \tilde{\mathbf{y}}_2]. \quad (38)$$

The calibrated confidence intervals for CQ-WNO can then be obtained as,

$$\mathcal{C}_p = [\tilde{\mathbf{y}}_1 - \mathbf{q}, \tilde{\mathbf{y}}_2 + \mathbf{q}]. \quad (39)$$

q is computed using a procedure similar to the one explained in Algorithm 1 with the exception that the base model is now Q-WNO and the score function corresponding to j^{th} element $y^{(j)}$ of the output vector \mathbf{y} is computed as,

$$e^{(j)} = \max\{\tilde{y}_1^{(j)} - y^{(j)}, y^{(j)} - \tilde{y}_2^{(j)}\}, \quad (40)$$

where $y_1^{(j)}$ and $y_2^{(j)}$ are the j^{th} elements of $y_1^{(j)}$ and $y_2^{(j)}$ respectively.

C Spiking Activity

In the various examples, the CRP-VSWNO networks are formed by using four VSNs in place of four continuous activations of CRP-WNO networks. Now to gauge the energy efficiency of VSNs, we report their spiking activity in Table 10. The idea here is that in event-driven hardware, reduced neuron activity will lead to reduced computations and, hence, more energy saving. For example, [27, 43] discuss that for VSNs to be energy efficient (compared to when using continuous activations) in synaptic operations of convolution layers, their spiking activity has to be less than 100%. It should be noted that in order to increase sparsity in communication during training, the spiking activity of the VSNs can also be penalized by incorporating the same in the loss function. The modified loss function L_s is termed as the Spiking Loss Function (SLF) and is defined as,

$$L_s = \alpha_w L_v + \beta_w S_a, \quad (41)$$

where L_v is the vanilla loss function like mean squared error and S_a is the total spiking activity ratio of all the VSNs, whose spiking activity needs to be constrained. The parameters α_w and β_w are the weights assigned to each loss function and the same act as hyper-parameters for the operator network. This can lead to marginal decrease in accuracy but the same can be managed by adopting appropriate weights in the loss function.

Table 10: Average spiking activity observed for various VSNs placed in RP-VSWNO networks. The reported spiking activity is calculated as the $100 \times$ number of spikes observed/ total possible spikes. The spiking activity is averaged over all samples of the test dataset and all models of the RP ensemble.

Example	VSN			
	1	2	3	4
E-I	30.27	22.90	16.16	3.05
E-II	44.87	33.04	10.19	5.88
E-III	34.87	38.03	23.84	4.90
E-IV (Real Component Network)	22.17	25.57	25.71	64.76
E-IV (Imaginary Component Network)	22.92	25.09	18.74	44.82